A General Ocean Color Atmospheric Correction Scheme Based on Principal Components Analysis - Part I: Performance on Case 1 and Case 2 Waters

Lydwine Gross-Colzy[1], Stéphane Colzy[2], Robert Frouin[3], Patrice Henry[4]
[1]Capgemini Space Unit, Toulouse, France; [2]Magellium, Ramonville Saint-Agne, France; [3]Scripps Institution of Oceanography, San Diego, California; [4]Centre National des Etudes Spatiales, Toulouse, France.

ABSTRACT

In order to retrieve ocean color from satellite imagery, one must perform atmospheric correction, because when observed from space the ocean signature is weak compared with the strong atmospheric signal. The color of the ocean depends on its optically active constituents: water molecules, dissolved matter, and particulate matter. In the open ocean, the color is mainly due to water molecules and phytoplankton, whereas in the coastal zone, the color also results from the presence of sediments and colored dissolved organic matter. Because coastal waters (Case 2 waters) are much more difficult to decouple from the atmosphere than open ocean (Case 1 waters), operational atmospheric correction algorithms usually separate Case 1 from Case 2 waters processing. The solution proposed in this paper does not separate them. Our algorithm, referred to as Ocean Color Estimation by principal component ANalysis (OCEAN), exploits the fact that ocean is more variable spectrally than the atmosphere, while the atmosphere signal is more variable in magnitude. The satellite reflectance is first decomposed into principal components. The components sensitive to the ocean signal are then combined to retrieve the principal components of the marine reflectance via neural network methodology. The algorithm is described, and results are presented on real and simulated data for POLDER, MERIS, SeaWiFS, and MODIS. Accurate water reflectance estimates are obtained for various aerosol types and contents (including maritime, coastal and urban mixtures), and for the full range of water properties (resulting from realistic combinations of chlorophyll content, sediment content, and colored dissolved matter absorption).

Keywords: Ocean color, chlorophyll, remote sensing, aerosols, atmospheric correction, principal component analysis, neural networks.

1. INTRODUCTION

Classic algorithms to estimate water-leaving reflectance from space[1-7] attempt to correct as accurately as possible the influence of the atmosphere on the top-of-atmosphere reflectance measured in the visible. The problem is difficult because only 10% of the signal measured at the ocean-color wavelengths (i.e., the useful signal) may originate from the water body[1-2]. The procedure consists of (1) estimating the aerosol reflectance in the red and near infrared where the ocean can be considered black (i.e., totally absorbing), and (2) extrapolating the estimated aerosol reflectance to shorter wavelengths. The retrieved water reflectance is then generally related to chlorophyll-a concentration using a bio-optical model, semi-analytical[8-9] or empirical[10]. This approach has been successful, and it is employed in the operational processing of data from most satellite ocean-color sensors. In coastal regions (about 2% of the global oceans), however, the assumption of null ocean reflectance in the red and near infrared is not valid, and improvements to the standard algorithms have been proposed. These improvements are based on assumptions of spatial homogeneity for the spectral ratio of the aerosol and water reflectance in the red and near infrared[11] or for the aerosol type[12].

Other algorithms[13-16] attempt to determine simultaneously aerosol properties and chlorophyll-a concentration. Through systematic variation of candidate aerosol models, phytoplankton scattering, chlorophyll-a concentration, and aerosol optical thickness, a best fit to the spectral top-of-atmosphere reflectance (visible and near infrared) is obtained in an iterative manner. The advantage of this approach, compared with the standard, two-step approach, resides in its ability to handle both weakly and strongly absorbing aerosols[15-16]. A drawback is that convergence may not be achieved immediately in some cases, making it difficult to process large amounts of satellite data. The approach is also limited by the difficulty to differentiate between aerosol absorption and water constituents like yellow substances, and the result may be noisy.

[1]lydwine.grosscolzy@capgemini.com, [2]stephane.colzy@magellium.fr, [3]rfrouin@ucsd.edu, [4]Patrice.Henry@cnes.fr.

Coastal Ocean Remote Sensing, edited by Robert J. Frouin, ZhongPing Lee,
Proc. of SPIE Vol. 6680, 668002, (2007) · 0277-786X/07/$18 · doi: 10.1117/12.738508

The two types of algorithms described above are fairly complicated. They require large look-up tables of aerosol optical properties or aerosol reflectance. These tables are called internally as the atmospheric correction (standard procedure or non-linear optimization) is effected. Among simple alternatives[17,18], we already proposed a solution in which the top-of-atmosphere reflectance spectra are linearly projected onto vectors forming an orthonormalized basis[17]. This basis is estimated by Principal Component Analysis on simulated top-of-the-atmosphere spectra, and allows to simply decouple atmosphere and ocean. The projections (also called the principal components) that are sensitive to the ocean signal are then combined to yield marine reflectance and chlorophyll-a concentration using neural network methodology. Neural-networks are useful here to deal with non-linearity and measurement noise.

Simulated data used to compute the vectorial basis may include urban, tropospheric, maritime and coastal aerosol mixtures, wide ranges of aerosol optical thickness, of geometric conditions and water constituents. We show that for hyperspectral sensors the methodology is applicable to Case 1 and Case 2 waters without distinction. Theoretical performance on water leaving reflectance is given in the visible and near-infrared regions for several current ocean-color sensors, from the Polarization and Directionality of the Earth's Reflectances sensor (POLDER, 6 bands), the Sea-viewing Wide Field-of-view Sensor (SeaWiFS, 8 bands), the Moderate Resolution Imaging Spectroradiometer (MODIS, 9 bands), to the Medium Resolution Imaging Spectrometer instrument (MERIS, 13 bands). The global root mean square error on the retrieved water reflectance is around 0.005 at 412 nm, 0.004 at 443 nm, 0.003 at 490 nm, 0.002 at 510, 560, and 620 nm, 0.001 at 665 and 708 nm, and below 0.0005 at longer wavelengths.

2. DATA SIMULATION

Instead of using radiance, L, we use reflectance defined as $\rho = \pi L/F_0 \cos(\theta_0)$, where F_0 is the extraterrestrial solar irradiance and θ_0 is the solar zenith angle. Neglecting the influence of direct sun glint and gaseous absorption for clarity, the top-of-atmosphere reflectance $\rho(\lambda)$ at wavelength λ can be expressed as

$$\rho(\lambda) = \rho_m(\lambda) + \rho_a(\lambda) + \rho_{ma}(\lambda) + t_m(\lambda)t_a(\lambda)[(1-f)\rho_w(\lambda) + f\rho_e(\lambda)] \quad (1)$$

where $\rho_m(\lambda)$ and $\rho_a(\lambda)$ are the pure molecule and aerosol-scattering contributions, respectively, $\rho_{ma}(\lambda)$ is the effect of molecule-aerosol interaction, $\rho_w(\lambda)$ is the water-body reflectance (just above the surface), $t_m(\lambda)$ and $t_a(\lambda)$ are diffuse transmittances due to molecules and aerosols, respectively, and f and ρ_e are the fraction of foam and the foam reflectance, respectively.

The molecular variables $\rho_m(\lambda)$ and $t_m(\lambda)$ can be computed precisely from atmospheric pressure and wind speed. One can therefore subtract $\rho_m(\lambda)$ from $\rho(\lambda)$ to form

$$\rho_p(\lambda) = \rho(\lambda) - \rho_m(\lambda) = \rho_a(\lambda) + \rho_{ma}(\lambda) + t_m(\lambda)t_a(\lambda)[(1-f)\rho_w(\lambda) + f\rho_e(\lambda)] \quad (2)$$

The atmospheric functions in Eq. (2) were simulated with a good spectral sampling rate (10 nm from 400 to 700 nm and then 20 nm until 1020 nm) using the CNES SOS radiation-transfer code[19] for a wide range of sun and view angles, aerosols, and wind speed. Sun and view zenith angles were varied randomly (uniform distribution in cosines) between 0 and 60° and 0 to 70°, respectively, relative azimuth angle from 0 to 180°, wind speed from 0 to 15 ms^{-1}, and aerosol optical thickness at 550 nm from 0.001 to 0.5 (uniform distributions). Four types of Shettle and Fenn[20] aerosol mixtures were considered, relative humidity was varied randomly from 40 to 99% (uniform distribution). The fraction of foam is computed in function of the wind speed[21] and the foam reflectance (supposedly isotropic), is taken from empirical data[21,22]. The water-body reflectance was simulated using a semi-empirical model:

$$\rho_w(\lambda) = 0.524 \times \pi/Q'(\lambda) \times 0.33 \times b_b(\lambda)/(a(\lambda) + b_b(\lambda)) \quad (3)$$

where a and b_b are the total absorption and total backscattering coefficients of the water body, respectively, Q' is an anisotropy factor[23,24], 0.524 stands for the water to air interface. We used two types of bio-optical modeling to simulate a and b_b, depending of the targeted sensor. For all sensors but MERIS, we used an average reflectance model for Case 1 waters based on chlorophyll-a concentration[9] (*Chla*), extended to various phytoplankton types by varying the backscattering and attenuation coefficients within published range[9,25]. The *Chla* concentration was logarithmically varied in the range 0.01-30 $mg.m^{-3}$. For MERIS, which number and distribution of bands allows the process of Case 2 waters, a three components modeling is used to simulate the water body, using chlorophyll-a (*Chla* from 0.01 to 30 $mg.m^{-3}$), sediments (*Sed* from 0.001 to 10 $mg.m^{-3}$), yellow substances absorption ($a_y(443)$ from 0.001 to 0.2 m^{-1})[26-32]. In practice, the SOS code was run twice for each case, once with aerosols, ρ_w, f, and ρ_e specified from the water-body reflectance

model and once without aerosols and $\rho_w(\lambda) = 0, f = 0$; $\rho_p(\lambda)$ was obtained as the difference between the two SOS top-of-atmosphere reflectance simulations. The effects of sun glint were included in the simulations. All the cases with a sun glint reflectance above 0.005 were discarded, which left 73279 realizations of geophysical observations for the analysis. Four ensembles of measurements was then created by applying the response of the different sensors filters to the simulated $\boldsymbol{\rho_w}$ and $\boldsymbol{\rho_p}$ spectra, and an estimation of each sensor measurement noise was added to the simulations: a random normally distributed bias (one bias is common to all bands of one simulation) in order to simulate absolute calibration incertitude (this bias allows also to take into account errors due to approximations made in the radiation transfer codes used to model the effects of whitecaps, sun glint, and Rayleigh scattering), and a random normally distributed and spectrally uncorrelated variable in order to simulate radiometric noise. For each $\boldsymbol{\rho_p}$ in the data ensemble, its noisy realization $\boldsymbol{\rho_p'}$ is defined by:

$$\rho_p'(\lambda) = \rho_p(\lambda)[1 + U\,\varepsilon_u(\lambda) + C\varepsilon_c] \quad (4)$$

where $\varepsilon_u(\lambda)$ and ε_c are random, Gaussian-distributed variables with a mean of zero and a variance of unity. The variable $\varepsilon_u(\lambda)$ represents the spectrally non-correlated noise and has a different realization for each band, while ε_c represents the spectrally correlated noise (the same for all bands). The parameters U and C are used to control the magnitude of the two types of noise. A previous study[17] showed that our algorithm is poorly sensitive to variations of C (global shifts) and thus poorly sensitive to absolute calibration. A simulated incertitude of 1% on the absolute calibration is sufficient for the algorithm to be applicable to real data, and thus we fixed C to 0.01 for each sensor. However, and as expected, the algorithm is sensitive to spectrally non-correlated noise (the spectral information is the main variable here). In the same previous study, we demonstrated that adding a pixel noise of 2% (U=0.02) to the simulated data was necessary to be able to process SeaWiFS imagery. We found this level of noise also adequate to MODIS and POLDER. For MERIS however, we used the spectral signal to noise ratio communicated by the ESA to compute U for each wavelengths which is under 1% for each band.

3. METHODOLOGY

Uncoupling the ocean from the atmosphere is achieved by a principal component analysis (PCA)[33] of a representative ensemble of $\boldsymbol{\rho_p}$ spectra, defined by their spectral bands only. The PCA creates an orthogonal basis constituted by the eigen-vectors of the variance-covariance matrices of the spectra ensemble (the eigen-vectors are extracted using a single decomposition technique, they are hereafter denoted as ***EIG-atm(i)***); then the eigen-vectors are classified using the magnitude of their associated eigen-values: the higher the magnitude, the more explained variance by the corresponding eigen-vector. Projections of $\boldsymbol{\rho_p}$ on the eigen-vectors are usually called principal components, and they are uncorrelated with each other. Because we defined sensor measurements by the spectral information only, the eigen-vectors reflect the spectral shapes encountered within these measurements (sign of the vectors are not to be taken into account though), and because we know that atmosphere has a smooth spectral behavior compared to ocean, we can expect that projecting $\boldsymbol{\rho_p}$ on their eigen-vectors will allow us to separate ocean from atmosphere.

For this study, we created a different basis for each sensor, each basis contains as much eigen-vectors as number of bands. Figure 1 shows the three first eigen-vectors of the $\boldsymbol{\rho_p}$ ensemble of each sensor. The first eigen-vector has a very smooth spectral shape, it shows that the signal magnitude is the first information contained by the $\boldsymbol{\rho_p}$ spectra. This eigen-vector does not allow one to uncouple atmosphere from ocean, but it is due in majority to the presence of aerosols ($\boldsymbol{\rho_a}$). The second eigen-vector has a blue signature, and is due in majority to multiple-diffusion in the atmosphere ($\boldsymbol{\rho_{ma}}$). The first and second eigen-vectors are thus strongly related to atmosphere, and the first and second principal components are subject to directionality, they are not to be used to retrieve ocean signal. On the contrary, the strong spectral shapes of the eigen-vectors starting from the third are to be related to ocean color.

To be consistent with the $\boldsymbol{\rho_p}$ decomposition, a PCA is also performed on the oceanic signal, and to respect the distribution of the simulated $\boldsymbol{\rho_w}$, the ***EIG-water(j)*** are computed on the covariance matrix of $\log10(\boldsymbol{\rho_w})$. Figure 2 shows the three first eigen-vectors of the $\log10(\boldsymbol{\rho_w})$ ensemble of each sensor. Using three eigen-vectors to estimate water signal allows us to reconstruct 99.9% of the variance of $\log10(\boldsymbol{\rho_w})$ for the one component ocean model (used for POLDER, SeaWiFS and MODIS) as for the three components ocean model (used for MERIS). The difference between the two models is the shape of the generated eigen-vectors.

In the following, we denote $\boldsymbol{cp_i}$, with $i = 1,\ldots n$ the principal components of $\boldsymbol{\rho_p}$, which are the projections of $\boldsymbol{\rho_p}$ onto its ***EIG-atm***:

$$cp_i = \boldsymbol{\rho_p} \,.\, \textbf{\textit{EIG-atm(i)}} \quad (5)$$

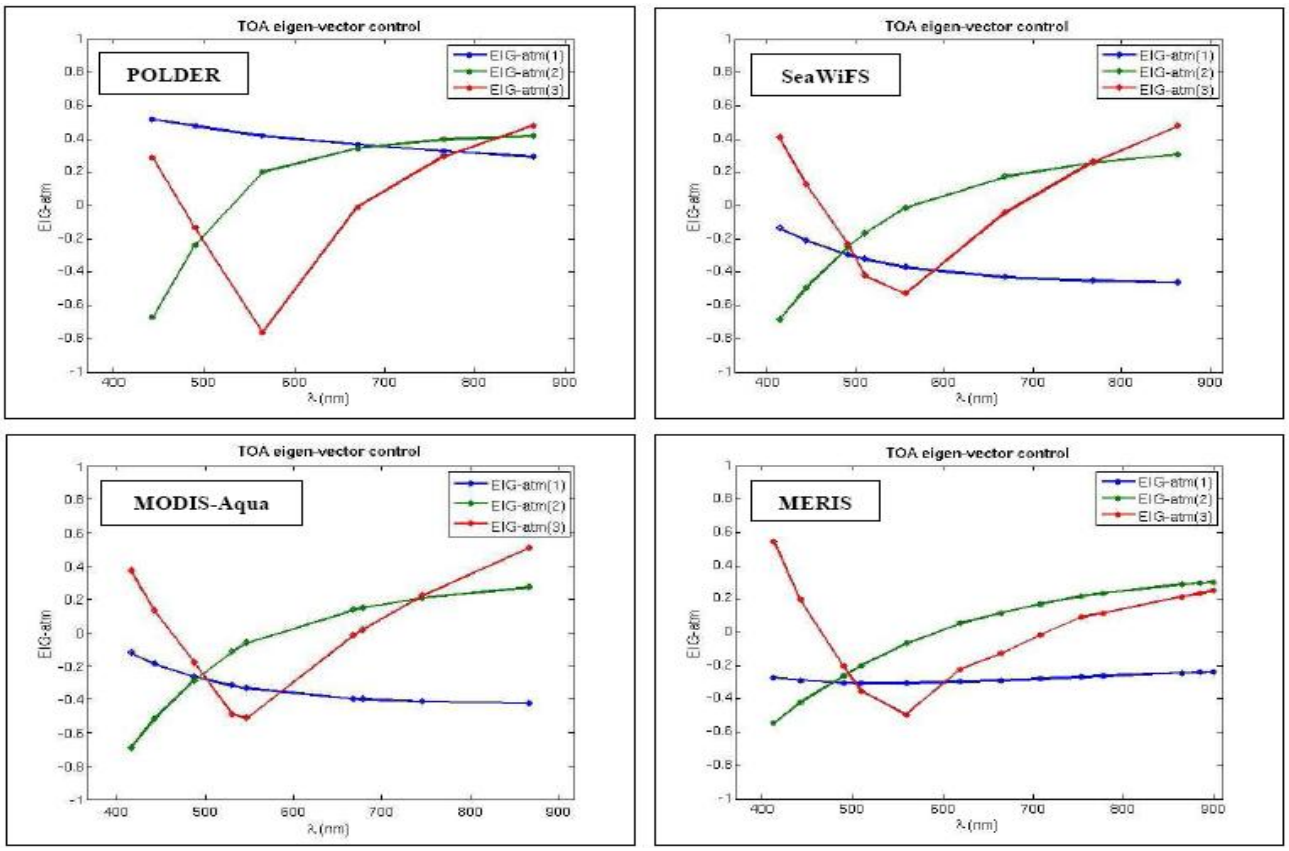

Figure 1. The three first eigen-vectors of ρ_p computed for each data ensemble (one per sensor). Spectral shapes are similar from a sensor to another.

Similarly, the principal components of ρ_w, denoted cw_j, with $j = 1,...,m$, are the projections of $\log10(\rho_w)$ onto its ***EIG-water***:

$$cw_j = \log10(\rho_w) \,.\, \textbf{\textit{EIG-water(j)}} \quad (6)$$

The signals have been linearized, and by inverting Eqs. (5) and (6) ρ_p and ρ_w can be written:

$$\rho_p = \sum_i cp_i \,.\, \textbf{\textit{EIG-atm(i)}} \quad (7)$$

$$\log10(\rho_w) = \sum_j cw_j \,.\, \textbf{\textit{EIG-water(j)}} \quad (8)$$

The linear correlation coefficients between the cp_i and the cw_j were computed for each data ensembles (Table 1, second column). The results indicate that it is possible to relate cw_j to cp_i via empirical relations and thus, that it is possible to perform a statistical atmospheric correction. Only the first three cw_j are required to reconstruct the ρ_w signal, since they gather 99.9% of the ρ_w ensemble variance. The ρ_w signal can be obtained from Eq. (8), in which the missing cw_j are fixed at their mean values, estimated on the data ensemble. Based on the correlation coefficients, empirical functions, f, g, and h are defined for each sensor (Table 1, third column). To avoid atmosphere and directionality, cp_1 and cp_2 are never used. To avoid noise measurement, cp_n (the last component) is never used.

Simple tests show that these multi-dimensional functions are non-linear. In order to approximate them, least-squared regressions are performed using neural-network modeling (multi-layered perceptrons, MLPs)[34]. Other universal function approximators are possible, but multi-layered perceptrons provide robust solutions when dealing with measurement noise. Note that the knowledge of cw_1 is absolutely necessary to reconstruct ρ_w, since it represents about 99% of the ocean signal variance. Indeed, in Case 1 waters, this component is directly related to the amount of chlorophyll-a in the ocean, *Chla*. Based on the data simulations, for Case 1 waters log10(*Chla*) can be computed from cw_1 using a second-order polynomial (Figure 3).

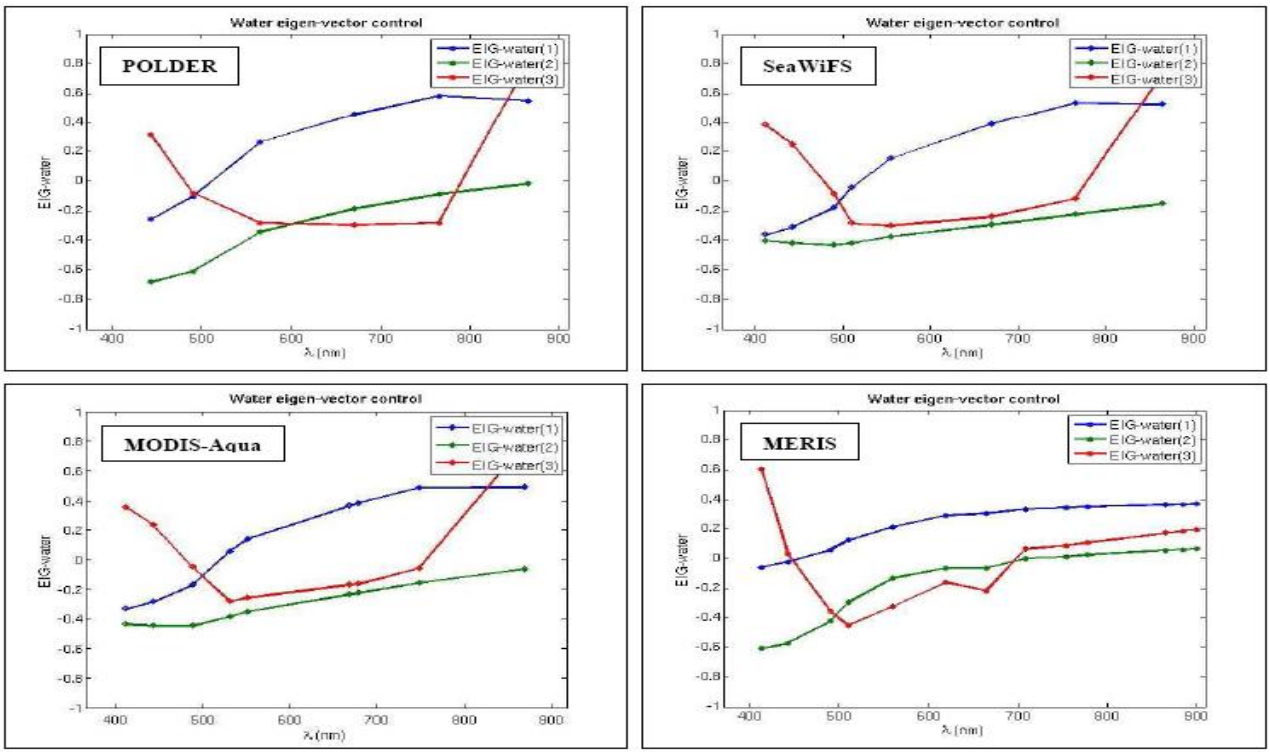

Figure 2. The three first eigen-vectors of log10(ρ_w) computed for each data ensemble (one per sensor). The eigen-vectors obtained on the MERIS ρ_w ensemble differ from the others because they correspond to a three components ocean model (chlorophyll, sediments, yellow substances) instead of a one component ocean model (chlorophyll).

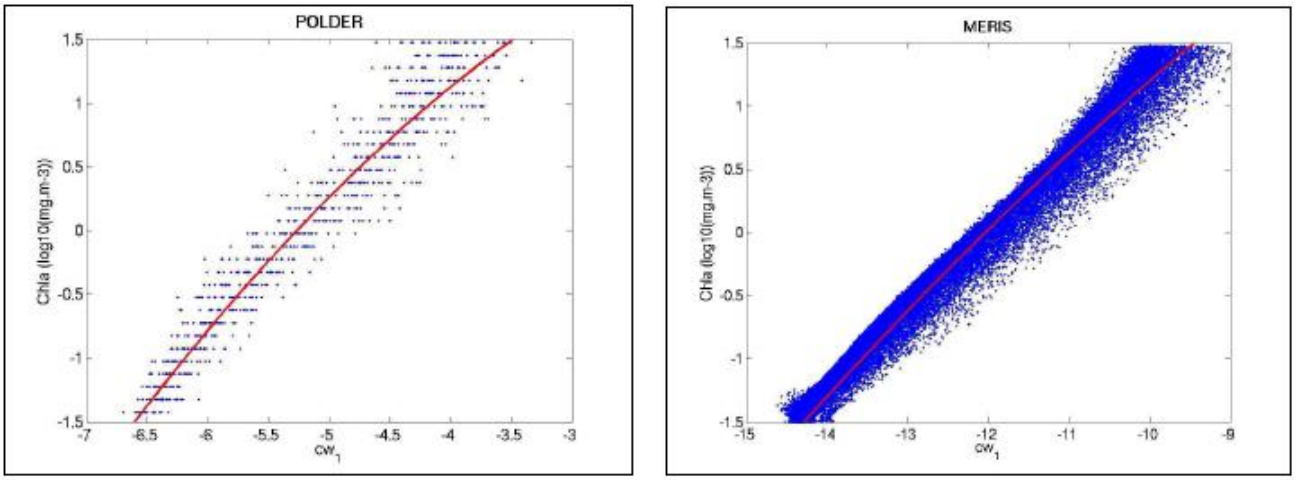

Figure 3. Relationship between the first component of log10(ρ_w) and log10(*Chla*), approximated by a second-order polynomial (in red). Left: case of POLDER (extended Case 1 waters, one component ocean model based on chlorophyll concentration), log10(*Chla*) = -0.0903 cw_1^2 + 0.0510 cw_1 + 2.7745. Right: case of MERIS (three components ocean model based on chlorophyll-a, sediments, yellow substances, in which sediments concentration and yellow substances are set to zero), log10(*Chla*) = -0.0179 cw_1^2 + 0.1934 cw_1 + 4.9254.

4. THEORETICAL RESULTS

Figure 4 displays scatter plots of retrieved versus desired cw_j (j = 1,…,3) for the entire SeaWiFS data ensemble (extended Case 1 waters) after calibration of the three functions (similar graph are obtained for the other sensors).

Retrievals of ρ_w, obtained by injecting retrieved cw_j into Eqs. 8, are displayed in Figures 5 for POLDER (6 bands, extended Case 1 waters) and MERIS (13 bands, Case 1 and Case 2 waters). The mean performance obtained on ρ_w for each sensor is given in Table 2.

Table 1. First column: sensor designation; Second column: correlation coefficients (%) between the principal components of ρ_p, cp_i, and the three first principal components of ρ_w, cw_j. Third column: empirical functions based on linear correlation matrix; Fourth column: canonical correlation k computed between the desired cw_j and the set of cp_i chosen to calculate it (%). The canonical correlation is the multi-dimensional linear correlation between the desired variable and the set of variables used to compute it. It gives the precision of the result if a linear least square regression is made to estimate the relation.

Sensor	Linear correlation matrix	Empirical functions	k (%)
POLDER	cp1 cp2 cp3 cp4 cp5 cp6		
	cw1 5.8 -39.1 -77.6 -25.8 -10.6 0.6	cw1 = f(cp3, cp4, cp5)	90.2
	cw2 8.1 -10.8 24.3 -24.2 29.7 4.4	cw2 = g(cp3, cp4, cp5)	65.4
	cw3 0.6 6.1 10.2 -58.4 24.5 -2.1	cw3 = h(cp3, cp4, cp5)	42.1
SeaWiFS	cp1 cp2 cp3 cp4 cp5 cp6 cp7 cp8		
	cw1 2.1 23.6 -59.4 -64.4 14.6 -13.2 -15.5 -4.5	cw1 = f(cp3, cp4, cp5, cp6, cp7)	91.1
	cw2 10.8 7.0 36.7 -8.2 -27.5 -53.9 -57.3 -2.3	cw2 = g(cp3, cp4, cp5, cp6, cp7)	91.4
	cw3 5.9 -12.7 31.3 -48.0 -54.1 39.6 13.5 -6.3	cw3 = h(cp3, cp4, cp5, cp6, cp7)	89.2
MODIS	cp1 cp2 cp3 cp4 cp5 cp6 cp7 cp8 cp9		
	cw1 0.5 23.7 -63.0 -64.6 -3.3 -1.3 -6.6 -2.0 4.2	cw1 = f(cp3, cp4, cp7)	90.5
	cw2 11.0 8.2 35.7 -17.3 33.9 31.2 -60.9 -11.3 12.3	cw2 = g(cp3, cp4, cp5, cp6, cp7, cp8)	86.8
	cw3 5.9 -12.4 28.0 -30.5 57.5 -44.8 27.6 1.0 -14.3	cw3 = h(cp3, cp4, cp5, cp6, cp7)	88.3
MERIS	cp1 cp2 cp3 cp4 cp5 cp6 cp7 cp8 cp9 cp10 cp11 cp12 cp13		
	cw1 -7.4 2.2 -72.6 -41.6 -23.4 -1.4 -3.2 -2.9 -1.2 -0.8 0.8 -0.4 -0.1	cw1 = f(cp3, cp4, cp5)	86.6
	cw2 11.5 22.6 4.9 30.9 -9.0 -4.1 -18.9 0.0 -2.8 -3.0 -0.1 0.5 0.2	cw2 = g(cp3, cp4, cp5, cp6, cp7, cp9,cp10)	38.0
	cw3 -0.4 1.1 18.1 27.8 -35.6 -5.7 6.5 0.6 -1.3 0.3 0.8 -0.4 0.1	cw3 = h(cp3, cp4, cp5, cp6, cp7)	49.1

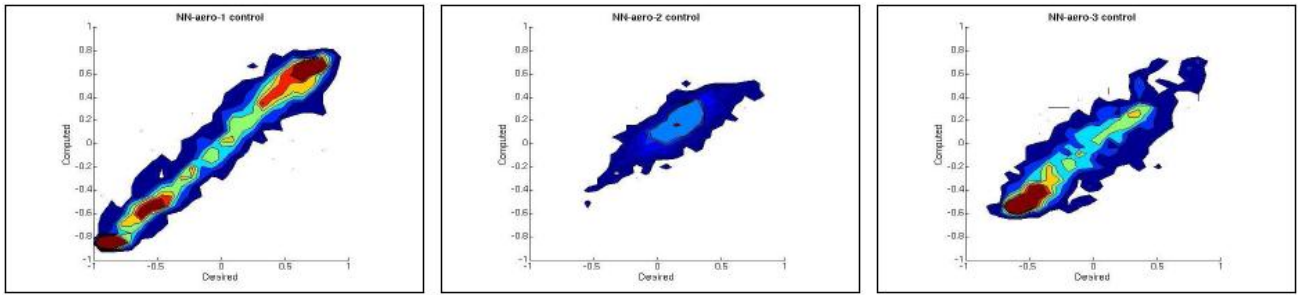

Figure 4. Scatter plots: retrieved ρ_w principal components using calibrated functions f, g, and h, plotted versus their desired values (SeaWiFS ensemble). The first component (left) is estimated with a mean accuracy of 2.95% and a correlation coefficient of 99%. The second component (middle) is estimated with a mean accuracy of 1.75% and a correlation coefficient of 90%. The third component (right) is estimated with a mean accuracy of 2.33% and a correlation coefficient of 93%. Thanks to the non-linearity introduced by the neural-networks, the correlation coefficients are better or equivalent than the canonical correlations (see Table 1). In the case of MODIS, correlation coefficients on retrieved cw_j are 97, 91, 92% for the first, second and third components respectively, for POLDER, 94, 81, 90%, for MERIS, 97, 94, 63%.

For extended Case 1 waters, best results are obtained for SeaWiFS, after comes MODIS, and then POLDER. It can be explained by the good spectral distribution of the eight SeaWiFS bands, while the fourth and fifth, and the sixth and seventh of the MODIS bands are very close, leading actually for the PCA to seven points spectra, rather than nine points spectra. The six bands of POLDER seem merely sufficient to retrieve the main spectral behavior of extended Case 1 waters, but we will see further than the directional information of POLDER (a pixel may be seen 12 times) allows to dramatically improve these results. RMS error decreases as the wavelengths increases, which is natural as variability and

magnitude of $\rho_w(\lambda)$ decreases from blue to NIR. Figure 6 shows the distribution of $\rho_w(443)$ relative error in function of atmospheric parameters and directionality for SeaWiFS (plots are equivalent for the other sensors). Performance of the inversion scheme is sensitive to the aerosol models and to the scattering angle, it is not sensitive to relative humidity, and a little sensitive to aerosol optical thickness: relative error slightly increases as aerosol optical thickness increases. For SeaWiFS, mean relative error is similar (around 11%) for the aerosols models tropospheric, urban and maritime, while it is around 15% for the coastal model. This can be explained by the fact that the coastal model is more absorbing than the others, and thus spectral information diminishes in presence of this type of aerosol mixture. We can also observe that better results are obtained for scattering angles between 120 and 140°, this is due to the distribution of the scattering angle in the data base used for the calibration of the empirical functions. Indeed by choosing the three directional parameters, solar zenith angle, viewing angle and azimuthal difference, by uniform random selection, we generated simulated scattering angles with a Gaussian distribution centered on 130°. And thus, because root mean square error minimization leads to conditional expectation, the empirical functions are centered on 130°. This aspect of the methodology may be adapted to each sensor viewing conditions. We can also notice that within the range 120-140° the aerosol phase function generally has its minimum, and thus the contribution of aerosols on ρ_p is easier to correct.

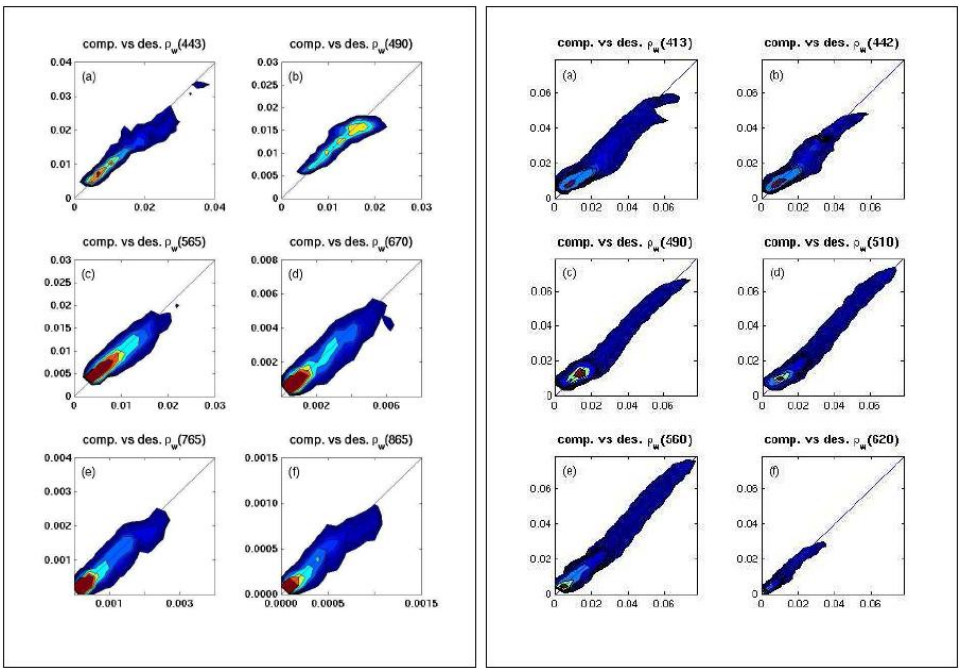

Figure 5. Retrieved six first bands of ρ_w plotted versus their desired values (left: POLDER: extended Case 1 waters, right: MERIS: Case 1 and Case 2 waters). Corresponding performance is given in Table 2.

Although for MERIS we used a more complex ocean model to simulate the data, performance is similar to what it is obtained on extended Case 1 waters, because the spectral sampling of MERIS allows us to detect a wide range of spectral variability (the MERIS empirical functions are more complex and much more non-linear than the functions of the other sensors, please compare the canonical correlations in Table 1 with the linear correlations obtained on water principal components in Figure 4 legend). RMS errors and bias are similar for Case 1 and Case 2 waters, only the relative errors made on $\rho_w(\lambda)$ are higher for Case 2 waters, because their values may be much more smaller, especially in the blue part of the spectrum. Figure 7 shows retrieved spectra compared to desired spectra in Case 1 and Case 2 waters at the MERIS wavelengths. Scatter plots of estimated versus desired *Chla* are displayed in Figure 8. Performance on Case 1 chlorophyll content is also indicated and corresponds to the biological noise we introduced in the modeling (variation of the phytoplankton type).

5. APPLICATION TO MERIS IMAGERY

In this paper we show the PCA-based neural network algorithm applied to MERIS (imagery acquired off California on November 16, 2002). Application to other sensors will be presented and discussed in the companion paper.

Table 2. Mean theoretical performance obtained on retrieved bi-directional reflectance ρ_w estimated by the empirical functions described in Table 1 (three for each sensor) followed by Eq. 8. Tests are done for the following geophysical conditions: chlorophyll range: 0.03 to 30.00 mg.m-^{3}, aerosol optical thickness at 550 nm: 0.00 to 0.30, Shettle & Fenn aerosol models: tropospheric, urban, maritime and coastal, humidity ratio: 40 to 99 %, solar zenithal angle: 0.00 to 60.00 degrees, viewing angle: 0.00 to 70.00 degrees, azimuthal difference: 0.00 to 180.00 degrees. For MERIS, Case 1 waters performance is obtained by testing on data in which sediments and yellow substance are set to zero, and Case 2 waters performance is obtained on data in which sediments concentration varies from 0.01 to 10 mg.m^{-3}, and yellow substances absorption at 443 nm varies from 0.005 to 0.2.

Sensor name / Type of water	Bands	RMS error		Relative error (%)		Linear Correlation (%)		Bias	
POLDER / extended Case 1 waters	ρ_w (443)	0.0051		20		87		0.0011	
	ρ_w (490)	0.0026		15		85		0.0005	
	ρ_w (565)	0.0022		15		93		0.0004	
	ρ_w (670)	0.0007		23		93		0.0001	
	ρ_w (765)	0.0004		29		92		0.0001	
	ρ_w (865)	0.0002		26		92		0.0000	
SeaWiFS / extended Case 1 waters	ρ_w (412)	0.0042		13		96		0.0009	
	ρ_w (443)	0.0030		12		96		0.0007	
	ρ_w (490)	0.0021		11		93		0.0006	
	ρ_w (510)	0.0014		9		92		0.0005	
	ρ_w (555)	0.0014		9		96		0.0004	
	ρ_w (670)	0.0003		12		98		0.0000	
	ρ_w (765)	0.0001		17		97		0.0000	
	ρ_w (865)	0.0001		17		97		0.0000	
MODIS / extended Case 1 waters	ρ_w (412)	0.0049		17		95		0.0009	
	ρ_w (443)	0.0034		15		94		0.0006	
	ρ_w (488)	0.0020		11		93		0.0005	
	ρ_w (531)	0.0012		8		95		0.0002	
	ρ_w (551)	0.0013		10		96		0.0000	
	ρ_w (667)	0.0006		20		93		-0.0001	
	ρ_w (678)	0.0005		21		93		-0.0001	
	ρ_w (748)	0.0003		29		91		-0.0001	
	ρ_w (869)	0.0001		27		92		0.0000	
MERIS / Case 1 & Case 2 waters / Case 1 waters	ρ_w (413)	0.0050	0.0053	26	17	95	96	0.0011	0.0023
	ρ_w (442)	0.0039	0.0035	21	17	95	94	0.0009	0.0009
	ρ_w (490)	0.0031	0.0023	16	14	97	70	0.0006	0.0003
	ρ_w (510)	0.0024	0.0018	14	12	98	89	0.0004	0.0004
	ρ_w (560)	0.0023	0.0014	14	12	99	97	0.0003	0.0003
	ρ_w (620)	0.0017	0.0008	20	18	97	95	0.0003	0.0000
	ρ_w (665)	0.0012	0.0005	21	19	97	94	0.0002	0.0000
	ρ_w (708)	0.0008	0.0004	24	21	96	93	0.0001	0.0000
	ρ_w (753)	0.0002	0.0001	25	23	96	93	0.0000	0.0000
	ρ_w (778)	0.0002	0.0001	26	23	96	93	0.0000	0.0000
	ρ_w (865)	0.0001	0.0001	28	25	96	93	0.0000	0.0000
	ρ_w (885)	0.0001	0.0001	29	26	96	93	0.0000	0.0000
	ρ_w (900)	0.0001	0.0000	29	26	96	93	0.0000	0.0000

A colored composition of ρ_w is showed on Figure 9 (California), where $\rho_w(665)$ stands for the red channel, $\rho_w(560)$ stands for the green channel, and $\rho_w(442)$ stands for the blue channel. The imagery seems not noisy; it allows a wide range of colors (from blue to red) and intensity (from low in the river plums, to bright in coastal areas). Vertical camera artifacts are still present though (MERIS SMILE effect). Figure 10 shows zooms of the resulting imaging in order to identify specific pixels, and Figure 11 shows associated spectra. The variability of the ρ_w spectra seems coherent with the oceanic structures and the associated *Chla* concentrations are reasonable.

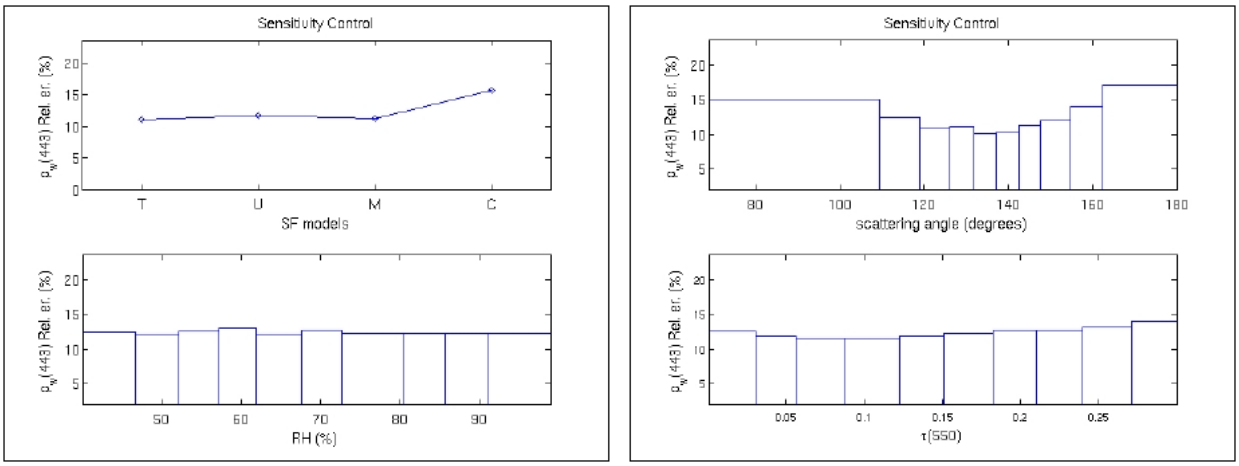

Figure 6. Distribution of the mean relative error obtained on $\rho_w(443)$ in function of Shettle & Fenn aerosol models (up-left, T: tropospheric, U: urban, M: maritime, C: coastal), relative humidity (down-left, RH), scattering angle (up-right), aerosol optical thickness at 550 nm (down-right, τ(550)).

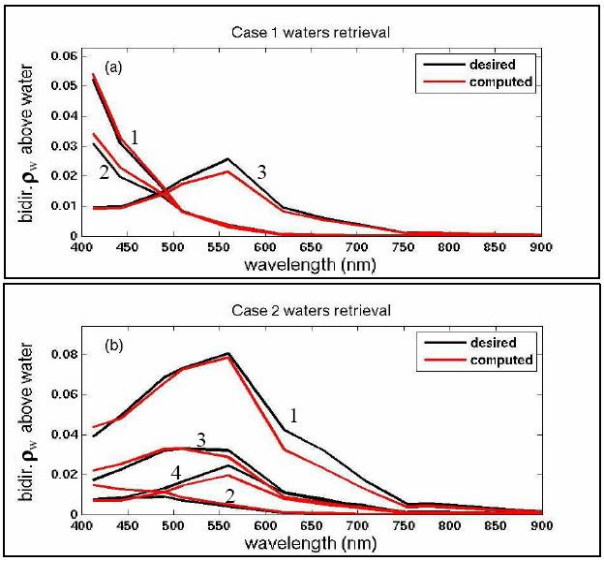

Figure 7. Bidirectional marine reflectance above water (MERIS wavelengths), comparison between desired and computed spectra for Case 1 waters ((a) 1: *Chla* = 0.03 mg.m^{-3}; 2: *Chla* = 0.1 mg.m^{-3}; 3: *Chla* =30 mg.m^{-3}) and Case 2 waters ((b) 1: *Chla*=0.01 mg.m^{-3}, *Sed*=10 mg.m^{-3}, $a_y(443)$=0.1; 2: *Chla*=0.1 mg.m^{-3}, *Sed*=0.2 mg.m^{-3}, $a_y(443)$=0.1; 3: *Chla*=4 mg.m^{-3}, *Sed*=3 mg.m^{-3}, $a_y(443)$=0.1; *Chla*=20 mg.m^{-3}, *Sed*=1 mg.m^{-3}, $a_y(443)$=0.03).

6. CONCLUSIONS

Atmospheric correction of satellite ocean color can be achieved effectively by decomposing ρ_p into principal components. The components that are sensitive to the ocean signal are combined to retrieve the principal components of ρ_w, allowing reconstruction of ρ_w and estimation of *Chla*. Neural network methodology is used to approximate the non-linear functions that relate the useful principal components of ρ_p to the principal components of ρ_w. The algorithm was theoretically tested on four sensors, with more and more spectral accuracy. The more spectral bands, the more variability of the ocean signal may be retrieved. The algorithm is able to perform atmospheric correction in a wide range of aerosol mixtures and whatever the water type, because the black pixel assumption is not necessary, acceptable theoretical performance is obtained both on marine reflectance and *Chla* concentration. When applied to MERIS imagery, it allows observing detailed structures, in shape and colors.

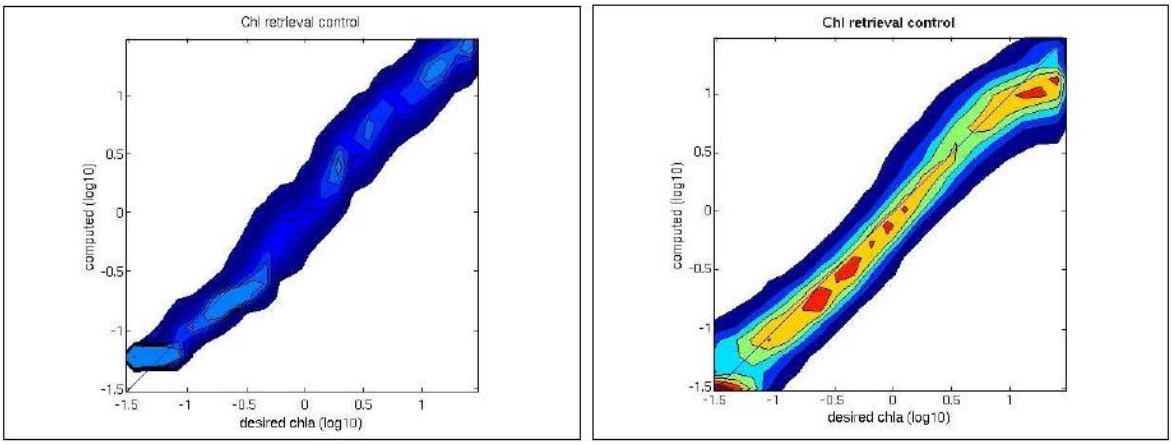

Figure 8. Scatter plots of retrieved Chla concentration versus desired (logarithmic scale). Left: SeaWiFS, global RMS error: 3.86 $mg.m^{-3}$, global relative error: 42%, linear correlation coefficient: 92%, bias: -1.19 $mg.m^{-3}$. Right: MERIS, global RMS error: 4.00 $mg.m^{-3}$, global relative error: 53%, linear correlation coefficient: 80%, bias: 0.7 $mg.m^{-3}$.

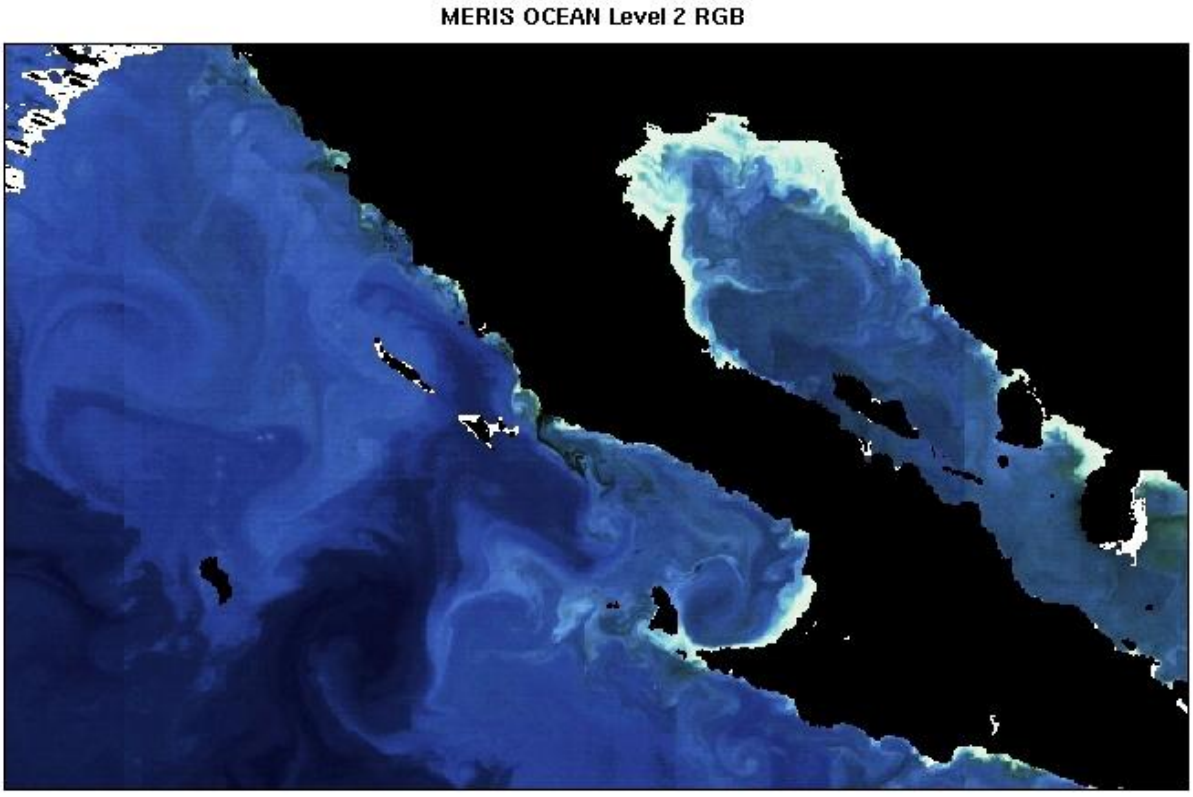

Figure 9. Colored composite of MERIS ρ_w, $\rho_w(665)$ stands for the red channel, $\rho_w(560)$ stands for the green channel, and $\rho_w(442)$ stands for the blue channel. For the imagery, the reflectance is encoded such as a 0 to 0.1 range becomes a 0 to 1 range.

ACKNOWLEDGMENTS

This work was supported by the Centre National des Etudes Spatiales and the National Aeronautics and Space Administration. The authors wish to thank J. McPherson from the Scripps Institution of Oceanography for technical support.

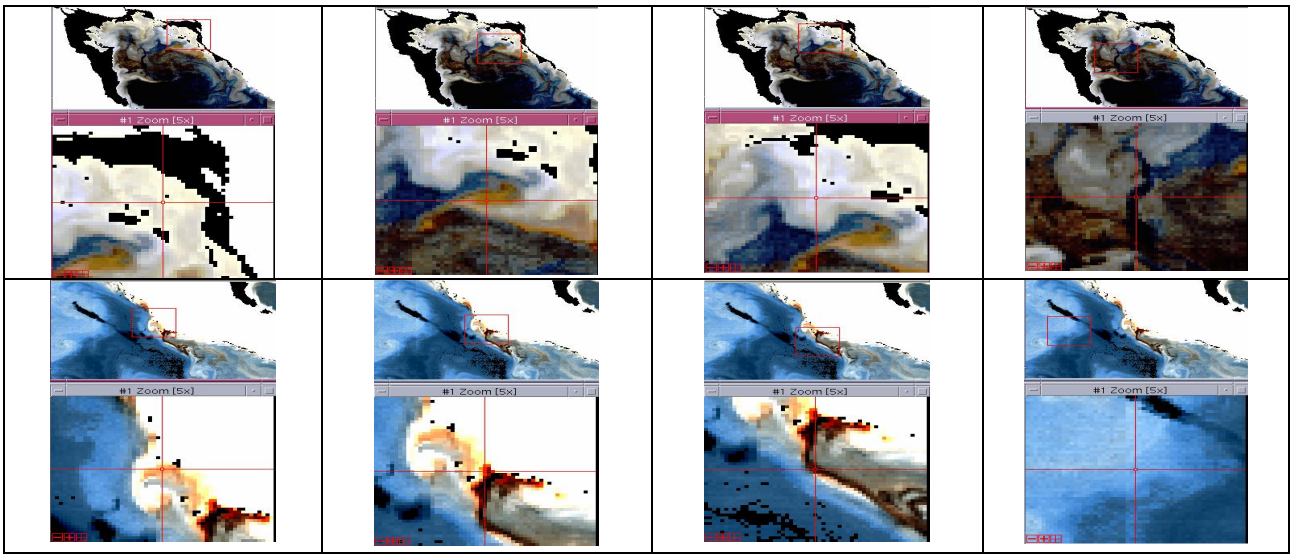

Figure 10. Zooms made with accentuated colors of the image of Figure 9. Top: Four pixels are identified in the Baja California Gulf. Bottom: Four pixels are identified in the Pacific Ocean.

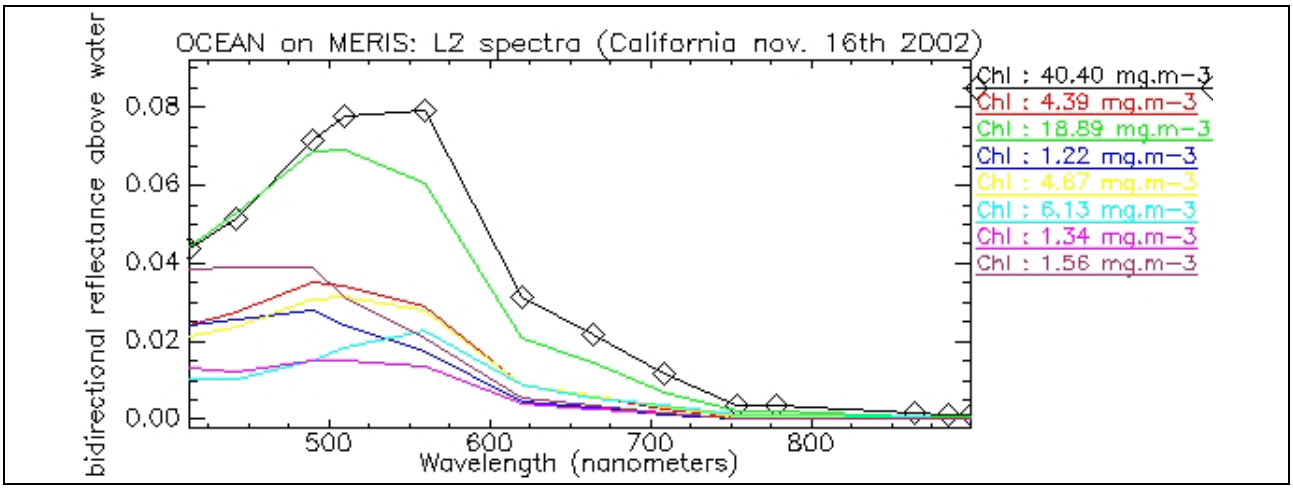

Figure 11. Bi-directional reflectance spectra ρ_w, taken on the image on Figure 9. The associated *Chla* concentrations are given by the MERIS Case 1 waters polynomial (Figure 3). The eight spectra from top to bottom on the legend correspond to the eight pixels identified on the small images of Figure 10, from top to bottom and from left to right.

REFERENCES

1. Gordon, H. R., "Removal of atmospheric effects from satellite imagery of the oceans", *Appl. Opt.*, **17**, pp. 1631-1636, 1978.
2. Viollier, M., D. Tanré, and P.-Y. Deschamps, "An algorithm for remote sensing of water color from space", *Boundary-Layer Meteor.*, **18**, pp. 247-267, 1980.
3. Gordon, H. R., and M. Wang, 1994, "Retrieval of water-leaving radiance and aerosol optical thickness over the oceans with SeaWiFS: a preliminary algorithm", *Appl. Opt.*, **33**, pp. 443-452, 1994.
4. Gordon, H. R., "Atmospheric correction of ocean color imagery in the Earth Observing System era", *J. Geophys. Res.*, **102**, pp. 17107-17118, 1997.
5. Fukushima, H., A. Higurashi, Y. Mitomi, T. Nakajima, T. Noguchi, T. Tanaka, and M. Toratani, "Correction of atmospheric effects on ADEOS/OCTS ocean color data: Algorithm description and evaluation of its performance", *J. Oceanogr.*, **54**, pp. 417-430, 1998.
6. Antoine, D., and A. Morel, "A multiple scattering algorithm for atmospheric correction of remotely sensed ocean colour (MERIS instrument): principle and implementation for atmospheres carrying various aerosols including absorbing ones", *Int. J. Remote Sens.*, **20**, pp. 1875-1916.

7. Gao, B.-C., M. J. Montes, Z. Ahmad, and C. O. Davis, "Atmospheric correction algorithm for hyper-spectral remote sensing of ocean color from space", *Appl. Opt.*, **39**, pp. 887-896, 2000.
8. Gordon, H. R., O. B. Brown, R. H. Evans, J. W. Brown, R. C. Smith, K. S. Baker, and D. K. Clark,"A semi-analytical radiance model of ocean color", *J. Geophys. Res*., **93**, 10909-10924, 1988.
9. Morel A., and S. Maritorena, "Bio-optical properties of oceanic waters: A reappraisal", *J. Geophys. Res*., **106**, 7163-7180, 2001.
10. O.Reilly, J. E., S. Maritorena, B. G. Mitchell, D. A. Siegel, K. L. Carder, S. A. Garver, M. Kahru, and C. McClain, " Ocean colour chlorophyll algorithms for SeaWiFS", *J. Geophys. Res*., **103**, 24937-24953, 1998.
11. Ruddick, K. G., F. Ovidio, and M. Rijkeboer, "Atmospheric correction of SeaWiFS imagery for turbid and inland waters", *Appl. Opt*., **39**, pp. 897-912,2000.
12. Hu, C., K. L. Carder, and F. Muller-Karger, "Atmospheric correction of SeaWiFS imagery over turbid coastal waters: A practical method. *Rem. Sens Environ*., **74**, pp. 195-206, 2000.
13. Land, P. E., and J. D. Haigh, "Atmospheric correction over case 2 waters using an iterative fitting algorithm", *Appl. Opt*., **35**, pp. 5443-5451, 1996.
14. Gordon, H. R., T. Du, and T. Zhang, Remote sensing of ocean color and aerosol properties: resolving the issue of aerosol absorption, *Appl. Opt.*, **36**, pp. 8670-8684, 1997.
15. Zhao, F., and T. Nakajima, "Simultaneous determination of water reflectance and aerosol optical thickness from Coastal Zone Color Scanner measurements, *Appl. Opt*., **36**, pp. 6949-6956, 1997.
16. Chomko, R., and H.R. Gordon, "Atmospheric correction of ocean color imagery: use of the Junge power-law aerosol size distribution with variable refractive index to handle aerosol absorption", *Appl. Opt.*, **37**, pp. 5560-5572, 1998.
17. L. S. Gross, and R. Frouin, "Remote sensing of chlorophyll concentration from space via principal component analysis of atmospherical effects", In Proc. SPIE Vol. 5155, Ocean Remote Sensing and Imaging II, R. Frouin, G. D. Gilbert, and D. Pan, Eds. (SPIE, Bellingham, WA), 112-123, 2004.
18. Frouin, R., L. Gross-Colzy, and P.-Y. Deschamps, "Ocean color remote sensing without explicit atmospheric correction", in Proceedings of SPIE Vol. 4892 *Ocean Remote Sensing and Applications*, edited by R. Frouin, Y. Yuan, and H. Kawamura, (SPIE, Bellingham, WA) pp. 133-142, 2003.
19. Deuzé, J.L., M. Herman, and R. Santer, "Fourier series expansion of the transfer equation in the atmosphere ocean system," *J. Quant. Spectrosc. Rad. Transfer*. **41** : 483-494, 1989.
20. Shettle, E.P., and R.W. Fenn, "Models for the aerosols of the lower atmosphere and the effect of the humidity variations on their optical properties," AFGL-TR-79-0214 no. 676, Air Force Geophys. Lab., Bedford, Mass., 1979.
21. Koepke, P., "Effective reflectance of oceanic whitecaps", *Appl. Opt.*, **23**, 1816-1824, 1984.
22. Fougnie B., and P.Y. Deschamps, "Observation et modélisation de la signature spectrale de l'écume de mer", 7th symposium of the International Society for Photogrametry and Remote Sensing, Courchevel, France, 7-11 avril 1997.
23. Morel, A. and B. Gentili, "Diffuse reflectance of oceanic waters: its dependence on Sun angle as influenced by the molecular scattering contribution", *Appl. Opt.*, **30**, 4427-4438, 1991.
24. Morel, A. and B. Gentili, "Diffuse reflectance of oceanic waters: II. Bidirectional aspects", *Appl Opt.*, **32**, 6864-6879, 1993.
25. Loisel, H. and A. Morel, "Light scattering and chlorophyll concentration in Case 1 waters, a reexamination", *Limn. and Oceanogr.*, **43**, 847-858, 1998.
26. Pope, R.M., and E.S. Fry, "Absorption spectrum (380-700nm) of pure water, II, Integrating cavity measurements" *Appl. Opt.*, **36**, 8710-8723, 1997.
27. Hale, G.M., and M.R. Querry, "Optical constants of water in the 200 nm to 200 micrometer wavelength region", *Appl. Opt.*, **12**, 555-565, 1973.
28. Bricaud et al., "Variability in the chlorophyll-specific absorption coefficients of natural phytoplankton: Analysis and parameterization", *J. Geophys. Res.*, **100**(C7), 13321-13332, 1995.
29. Bricaud et al., "Variations of light absorption by suspended particles with the chlorophyll-a concentration in oceanic (case 1) waters: Analysis and implications for bio-optical models", *J. Geophys. Res.*, **103**, 31033-31044, 1998.
30. Babin et al., "Variations in the light absorption coefficients of phytoplankton, non-algual particles, and dissolved organic matter in coastal waters around Europe", *J. Geophys. Res.*, **108** (C7), 3211-, 2003.
31. Morel, A., "Optical properties of pure water and pure sea water", Optical Aspects of Oceanography, N.G. Jerlov and E.S. Nielsen, eds. (Academic, New-York, 1974), pp. 1-24.
32. Babin et al., "Light scattering properties of marine particles in coastal and oceanic waters as related to the mass concentration", *Limn. and Oceanogr.*, **48**, 843-859, 2003.
33. Jollife, I. T., "Principal component analysis", Springer-Verlag, New York, 1986.
34. Bishop, C. M., "Neural networks for pattern recognition", Clarendon Press, Oxford, 1997.